

First-principles calculation of lattice thermal conductivities of α -, β -, and γ - Si_3N_4

Kazuyoshi Tatsumi,^{1,2,*} Atsushi Togo,² and Isao Tanaka^{2,3,4}

¹Advanced Measurement Technology Center, Institute of Materials and Systems for Sustainability, Nagoya University, Chikusa, Nagoya 464-8603, Japan

²Center for Elements Strategy Initiative for Structural Materials, Kyoto University, Sakyo, Kyoto 606-8501, Japan

³Department of Materials Science and Engineering, Kyoto University, Sakyo, Kyoto 606-8501, Japan

⁴Nanostructures Research Laboratory, Japan Fine Ceramics Center, Atsuta, Nagoya 456-8587, Japan

Lattice thermal conductivities of α -, β - and γ - Si_3N_4 single crystals are investigated from *ab initio* anharmonic lattice dynamics, within the single-mode relaxation-time approximation of the linearized phonon Boltzmann transport equation. At 300 K, the lattice thermal conductivity of β - Si_3N_4 is calculated as $\kappa_{xx} = 73$ and $\kappa_{zz} = 198$ (in units of $\text{Wm}^{-1}\text{K}^{-1}$), that is consistent with the reported experimental values of 69 and 180, respectively. For α - Si_3N_4 , $\kappa_{xx} = 69$ and $\kappa_{zz} = 99$ are obtained. The difference of anisotropy between these phases is originated from their characteristic difference in the phonon band structures, closely connected to the crystal structures, specifically, the stacking orders of equivalent basal layer structures. In α - Si_3N_4 , acoustic-mode phonons below 6 THz are the main heat carriers. In β - Si_3N_4 , the phonon modes up to 12 THz contribute to the lattice thermal conductivity. In γ - Si_3N_4 , $\kappa = 81$ is obtained. The distribution of phonon mode contributions to lattice thermal conductivity with respect to phonon frequency is found to closely resemble the distribution for the κ_{xx} of β - Si_3N_4 although the phonon lifetimes of γ - Si_3N_4 are twice shorter than those of β - Si_3N_4 .

I. INTRODUCTION

Several nitride insulators are known to exhibit high thermal conductivities and are important for heat transfer materials at elevated temperatures. For example, Slack *et al.*¹ reported that wurtzite-type AlN has thermal conductivity exceeding $100 \text{ Wm}^{-1}\text{K}^{-1}$. Si_3N_4 has become another promising thermal conductive insulator as its thermal conductivity has been improved up to $177 \text{ Wm}^{-1}\text{K}^{-1}$ by using the advanced ceramic technologies related to the densification and microstructure control.^{2–5} Since the Si_3N_4 ceramics also exhibit high mechanical strength at elevated temperatures, they are regarded as ideal materials for the use in various applications, such as engine components, gas turbines, and heat sink substrates of power semiconductor devices.

At atmospheric pressure, Si_3N_4 exists in one of two phases, α and β , which are generally considered as low- and high-temperature phases, respectively.^{2,5,6} Their crystal structures belong to the space groups of P31c and P6₃/m, respectively.^{7,8} These structures have different stacking orders of equivalent basal layer structures originated by SiN_4 tetrahedra.⁹ In Fig. 1 these layer structures are depicted from the principal direction, as A, B, C, and D in the α phase and A and B in the β phase. The stacking manners in α - and β - Si_3N_4 are thus as ABCDABCD.. and ABAB.., respectively. The α phase has additional two layer structures of C and D, which are related to the A and B by the *c* glide operation.⁹ Along this direction the lattice constant of the α phase is approximately twice longer than that of the β phase.

The reported values^{2–5,11} of the thermal conductivity of the Si_3N_4 polymorphs were measured on polycrystalline bulk samples. These values were significantly af-

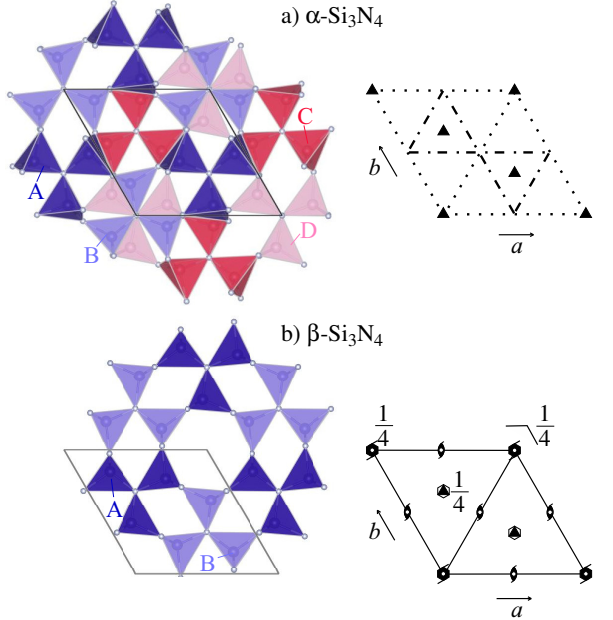


FIG. 1. (color online) Crystal structures of α - and β - Si_3N_4 . Stacking of SiN_4 tetrahedron layers are shown in left. (a) ABCDABCD.. for α - Si_3N_4 . (b) ABAB.. for β - Si_3N_4 . Space group diagrams¹⁰ in P31c (α - Si_3N_4) and P6₃/m (β - Si_3N_4) are shown in right.

fected by the lattice defects, impurities, shapes and orientations of the constituent crystal grains;¹² the thermal conductivity intrinsic to a defect-free single crystal has not been established. As an experimental approach to the intrinsic thermal conductivity, Li *et al.*¹³ applied high-resolution thermoreflectance microscopy to single β -

Si_3N_4 grains in a ceramic sample. The analyzed thermal conductivities were 69 and $180 \text{ Wm}^{-1}\text{K}^{-1}$ along the a and c axes, respectively. These thermal conductivities correspond to the xx and zz elements of the lattice thermal conductivity tensor κ . We consider the anisotropy of $\kappa_{zz}/\kappa_{xx} \sim 3$ is relatively large. Theoretically, Hiroasaki *et al.*¹² estimated κ by applying the Green-Kubo formulation to the molecular dynamics (MD) method with the interatomic potentials proposed by Vashishta *et al.*¹⁴. They calculated κ_{xx} and κ_{zz} of $\alpha\text{-Si}_3\text{N}_4$ as 105 and $225 \text{ Wm}^{-1}\text{K}^{-1}$, and those of $\beta\text{-Si}_3\text{N}_4$ as 170 and $450 \text{ Wm}^{-1}\text{K}^{-1}$, respectively. The ratio κ_{zz}/κ_{xx} in $\beta\text{-Si}_3\text{N}_4$ agreed well with the experimental one: The κ_{ii} values overestimated the experimental ones by more than two times.

On many polymorphs of the wurtzite and zincblende structures, the lattice thermal conductivities were recently calculated based on a first principles calculation and Boltzman transport theory.¹⁵ These crystal structures have different stacking orders of the densest atom planes as ABAB.. and ABCABC... The different stacking orders merely altered the lattice thermal conductivities.¹⁵ The phonon linewidth distribution and phonon density of states were similar between the structures as well.¹⁵ On the other hand, the previous MD results on α - and $\beta\text{-Si}_3\text{N}_4$ presented that the different stacking orders in these phases altered κ largely. This has not been explained through the phonon properties. It is interesting to investigate it using the same approach as in Ref.15.

In addition to the α and β phases, a cubic spinel phase ($\gamma\text{-Si}_3\text{N}_4$) is known to form upon compression and in-situ heating.^{16,17} The reported transition pressures were scattered from 10 to 36 GPa depending on the experimental conditions.¹⁸ The γ phase is experimentally quenched to atmospheric pressure at room temperature. Its thermal conductivity has not been experimentally reported; it has been estimated only by the Slack model.¹⁹

The present study aims to qualitatively understand the lattice thermal conductivity tensors among the three Si_3N_4 phases by means of the first principles approach. We calculate κ of the γ phase as well, for systematic understanding of the lattice thermal conductivity in the Si_3N_4 system. After the methodology section, we examine the validity of the present results first. Our calculated thermal properties are compared with the available experimental and theoretical references. Then we investigate the characteristics in the calculated κ in detail on the basis of the phonon band structures and phonon linewidths.

II. COMPUTATIONAL PROCEDURES

A. Lattice thermal conductivity calculation

The lattice thermal conductivities were calculated by solving the linearized Boltzmann transport equation (LBTE) within the single-mode relaxation time approx-

imation (single-mode RTA). We also tried the direct solution of LBTE²⁰ and leave its calculated κ values in the following section. The differences between the κ calculated by the single-mode RTA and the direct solution were found minor for our discussion. Therefore we limited our research to use the single-mode RTA to take advantage of its intuitive closed form of κ .

In the following sections, we denote a phonon mode by $\lambda = (\mathbf{q}, p)$ with the set of the phonon wave vector \mathbf{q} and band index p and $-\lambda \equiv (-\mathbf{q}, p)$. The relaxation time due to phonon-phonon scattering was obtained as reciprocal of linewidth, $\tau_{\lambda, \text{ph-ph}} = (2\Gamma_{\lambda})^{-1}$, where the linewidth that we employed in this study is as follows:

$$\begin{aligned} \Gamma_{\lambda} = & \frac{18\pi}{\hbar^2} \sum_{\lambda' \lambda''} |\Phi_{-\lambda \lambda' \lambda''}|^2 \times \\ & \{(n_{\lambda'} + n_{\lambda''} + 1)\delta(\omega_{\lambda} - \omega_{\lambda'} - \omega_{\lambda''}) + \\ & (n_{\lambda'} - n_{\lambda''})[\delta(\omega_{\lambda} + \omega_{\lambda'} - \omega_{\lambda''}) - \delta(\omega_{\lambda} - \omega_{\lambda'} + \omega_{\lambda''})]\}. \end{aligned} \quad (1)$$

Here ω_{λ} is the harmonic phonon frequency of the phonon mode λ , $n_{\lambda} = [\exp(\hbar\omega_{\lambda}/k_B T) - 1]^{-1}$ is the Bose-Einstein distribution at temperature T , and $\Phi_{\lambda \lambda' \lambda''}$ denotes the three-phonon-scattering strength. $\Phi_{\lambda \lambda' \lambda''}$ was obtained by usual coordinate transformation of third-order force constants from direct space to phonon space.¹⁵ The second- and third-order real-space force constants were obtained from the *ab-initio* calculation, whose details are written in the next section.

In order to compare the more realistic results of the calculated κ with the experimental data, the isotopic scattering effect due to the natural isotope distribution was taken into account according to the second-order perturbation theory.²¹ With the relaxation times of the phonon-phonon scattering and isotopic scattering, $\tau_{\lambda, \text{ph-ph}}$ and $\tau_{\lambda, \text{iso}}$, the total relaxation time for a phonon mode was assumed to be $1/\tau_{\lambda} = 1/\tau_{\lambda, \text{ph-ph}} + 1/\tau_{\lambda, \text{iso}}$, according to Matthiessen's rule.

The available experimental thermal conductivity data of the Si_3N_4 system have been measured on the polycrystalline samples and not measured from any single crystals. In order to consider the effect of various lattice defects in the polycrystalline samples, such as grain boundaries, impurities, and vacancies, we crudely took them into account by a relaxation time $\tau_{\lambda, \text{bs}} = L/|\mathbf{v}_{\lambda}|$ of a phonon boundary scattering model, where $\mathbf{v}_{\lambda} = \nabla_{\mathbf{q}}\omega_{\lambda}$ is the group velocity and L a parameter regarding to the boundary mean free path. We consider $\tau_{\lambda, \text{bs}}$ as a variable parameter and included it to κ according to Matthiessen's rule.

The closed form of κ within RTA was obtained via

$$\kappa(T) = \frac{1}{N_{\mathbf{q}} \Omega} \sum_{\lambda} \tau_{\lambda}(T) \mathbf{v}_{\lambda} \otimes \mathbf{v}_{\lambda} c_{\lambda}(T), \quad (2)$$

where $N_{\mathbf{q}}$ is the number of \mathbf{q} -points, Ω is the unit cell volume, and c_{λ} is the mode heat capacity. To analyze κ in

detail, we calculate the cumulative thermal conductivity:

$$\boldsymbol{\kappa}^c(\omega) = \frac{1}{N_{\mathbf{q}}\Omega} \int_0^\omega \sum_\lambda \tau_\lambda(T) \mathbf{v}_\lambda \otimes \mathbf{v}_\lambda c_\lambda(T) \delta(\omega' - \omega) d\omega', \quad (3)$$

and its derivative $\frac{\partial \boldsymbol{\kappa}^c(\omega)}{\partial \omega}$ to see the phonon mode contributions to $\boldsymbol{\kappa}$.

The lattice thermal conductivities were calculated with the phonon-phonon interaction calculation code PHONO3PY¹⁵, while the harmonic phonon states were analyzed with the phonon calculation code PHONOPY²².

B. Computational details

The force constants were calculated using the first-principles projector augmented wave method²³ (VASP code^{24–26}). The generalized gradient approximation (GGA) parameterized by Perdew, Burke, and Ernzerhof²⁷ was used for the exchange correlation potential. A plane wave energy cutoff of 500 eV was employed. The crystal structures were optimized until the residual forces acting on the constituent atoms were less than 10^{-6} eV/Å. The structural optimization was firstly performed for a temperature of 0 K and 0 GPa. Here the temperature and pressure were considered only for the electronic system and the zero point lattice vibration was not taken into account. The calculated lattice parameters were $a = 7.808$ Å and $c = 5.659$ Å for the α phase, $a = 7.660$ Å and $c = 2.925$ Å for the β phase, and $a = 7.787$ Å for the γ phase, which agree with the experimental data^{7,8,28} within $+0.7\%$ errors. The lattice volume optimized within the local density approximation (LDA)²⁹ for the exchange correlation potential was, for $\beta\text{-Si}_3\text{N}_4$, 3 % smaller than within GGA, which is a typical volume contraction of LDA. The $\boldsymbol{\kappa}$ calculated within LDA was larger by 2.6 % than within GGA. For our discussion, this difference is enough small, therefore the impact of choice of exchange correlation potential is considered to be minor in our study.

Supercell and finite difference approaches were used to calculate the force constants.³⁰ The supercells were $1 \times 1 \times 2$, $1 \times 1 \times 3$, and $1 \times 1 \times 1$ supercells of the conventional unit cells for the calculation of the third-order force constants in α , β , and $\gamma\text{-Si}_3\text{N}_4$, respectively. Those were $3 \times 3 \times 4$, $3 \times 3 \times 8$ and $2 \times 2 \times 2$ for the second-order force constants. The length of the induced atomic displacement was set to 0.03 Å. Table I shows the $\boldsymbol{\kappa}$ calculated with several different sets of the supercells, indicating that our calculated $\boldsymbol{\kappa}$ is reasonably converging with respect to the size of the supercells.

Non-analytical term correction³¹ was applied to the second-order force constants to take into account the long range Coulomb forces present in ionic crystals. For the correction, static dielectric constants and Born effective charges were calculated by using the density func-

TABLE I. Calculated lattice thermal conductivities of α -, β -, and $\gamma\text{-Si}_3\text{N}_4$ ($\text{WK}^{-1}\text{m}^{-1}$) at 300 K with respect to several combinations of supercell sizes.

Phase	Supercell (# of atoms)		LTC	
	3 rd force constants	2 nd force constants	<i>xx</i>	<i>zz</i>
α	1 \times 1 \times 1 (28)	1 \times 1 \times 1 (28)	37	57
	1 \times 1 \times 2 (56)	1 \times 1 \times 2 (56)	41	79
	1 \times 1 \times 1 (28)	2 \times 2 \times 2 (224)	55	81
	1 \times 1 \times 2 (56)	2 \times 2 \times 2 (224)	67	95
	1 \times 1 \times 2 (56)	2 \times 2 \times 3 (336)	68	97
β	1 \times 1 \times 2 (56)	3 \times 3 \times 4 (1008)	68	100
	1 \times 1 \times 2 (28)	1 \times 1 \times 2 (28)	44	173
	1 \times 1 \times 2 (28)	2 \times 2 \times 4 (224)	76	208
	1 \times 1 \times 3 (42)	2 \times 2 \times 4 (224)	71	194
	1 \times 1 \times 3 (42)	2 \times 2 \times 5 (280)	72	196
γ	1 \times 1 \times 3 (42)	3 \times 3 \times 8 (1008)	73	199
	1 \times 1 \times 1 (56)	1 \times 1 \times 1 (56)	72	
	1 \times 1 \times 1 (56)	2 \times 2 \times 2 (448)	77	
	1 \times 1 \times 1 (56)	3 \times 3 \times 3 (56)	79	

tional perturbation theory (DFPT) as implemented in the VASP code^{32,33}.

Uniform \mathbf{k} -point sampling meshes of $4 \times 4 \times 2$, $4 \times 4 \times 3$, and $3 \times 3 \times 3$ were used for the third-order force constants of the α , β , and γ phases. For the α and β phases the center of the a^*b^* plane was sampled while the center on the c^* -axis was not. For the γ phase, non- Γ center mesh was used. For the second-order force constants, the Γ -point was only sampled for the α and β phase and the only one $\mathbf{k} = (0.5, 0.5, 0.5)$ point was sampled for the γ phase. The \mathbf{q} -point sampling meshes of $10 \times 10 \times 14$, $10 \times 10 \times 26$, and $12 \times 12 \times 12$ were used to calculate $\boldsymbol{\kappa}$ in Eq. (2) for the α , β , and γ phases.

We examined the effect of thermal expansion on $\boldsymbol{\kappa}$. For this, we calculated the $\boldsymbol{\kappa}$ with the crystal structures optimized for several finite temperatures within the quasi-harmonic approximation (QHA)³⁴. These $\boldsymbol{\kappa}$ were different from the $\boldsymbol{\kappa}$ for the corresponding temperatures, calculated with the structure initially optimized for 0 K. We consider these differences as the effect of thermal expansion. For $\beta\text{-Si}_3\text{N}_4$ and temperatures of 300, 600, 900, 1200, and 1500 K, the differences were found less than 1 %, similar to the case of Si and Ge³⁵. For the present study, these differences are negligible and we adopt the $\boldsymbol{\kappa}$ calculated with the structure initially optimized for 0 K.

In addition, we calculated the volumetric thermal expansion coefficients. Their comparison with the experimental coefficients is useful to validate the present thermal conductivity calculation, because the thermal expansion is originated from the anharmonicity of the interatomic potential as well as $\boldsymbol{\kappa}$. The calculated coefficients of the α and β phases are 4.31×10^{-6} and 4.19×10^{-6} K⁻¹ for 300 K, while the experimental values³⁶ were

3.75×10^{-6} and $3.55 \times 10^{-6} \text{ K}^{-1}$). The present calculation reproduced the experimental tendency where the α phase has a slightly larger thermal expansion coefficient than the β phase, supporting that the present calculations enable us to qualitatively compare the calculated κ among the Si_3N_4 phases.

In order to compare the microscopic phonon properties among the three phases at the same conditions, those results calculated at 0 GPa are shown and discussed. For the γ phase, this means that we assume the condition of a virtually quenched γ phase at 0 GPa from the high pressure. To examine the analytical continuity of the properties with respect to pressures, we calculated κ of the γ phase at 10, 20, and 40 GPa as shown in Fig. 8. The phenomenological behaviour of linear dependence of κ with respect to pressure was reproduced as similar to Ref. 37. The slope was $2.89 \text{ Wm}^{-1}\text{K}^{-1}\text{GPa}^{-1}$ for the γ phase. By this dependence, we consider that the microscopic values are also varied smoothly with the pressure and those at 0 GPa are valuable to compare with the α and β phases.

C. Direct solution of LBTE

The merit to employ the single-mode RTA for thermal conductivity calculation is the closed form, by which we can intuitively understand the qualitative character of κ in terms of the relaxation time and group velocity. The microscopic understanding of the full solution of LBTE is still under the development³⁸ and the microscopic picture based on collective phonons³⁹ will require more complicated investigation although it is known that the single-mode RTA solution of LBTE often underestimates the full solution.^{35,40}

For the α and β phases, we calculated κ by a direct solution of LBTE²⁰, which is one of the methods of LBTE full solutions. Their κ_{xx} and κ_{zz} without the isotope effect were 69 and $102 \text{ Wm}^{-1}\text{K}^{-1}$ for the α phase and 76 and $238 \text{ Wm}^{-1}\text{K}^{-1}$ for the β phase, respectively, while the corresponding single-mode RTA values were 70 and $102 \text{ Wm}^{-1}\text{K}^{-1}$ for the α phase and 76 and $210 \text{ Wm}^{-1}\text{K}^{-1}$ for the β phase. The κ_{zz} of the direct solution in the β phase was 13 % larger than that of the single-mode RTA solution. Since the differences in κ between the LBTE solutions are not significant, we expect the physics on those lattice thermal conductivities is well understood within RTA in the current level of our interest. Therefore, we discuss the lattice thermal conductivities using the results of the single-mode RTA solution.

III. RESULTS AND DISCUSSION

A. Lattice thermal conductivities

Table II shows the present results of the κ for 300 K. β - Si_3N_4 has a markedly more anisotropic κ than α - Si_3N_4 .

TABLE II. Calculated thermal conductivities of α - Si_3N_4 (trigonal), β - Si_3N_4 (trigonal), and γ - Si_3N_4 (cubic) at 300 K, compared with the experimental data. Theoretical bulk moduli B in units of GPa, calculated by the authors by using the present band method, are presented in the fourth column.

	This work		κ	Ref. Theo.		Ref. Expt.	
	κ_{xx}	κ_{zz}		κ_{xx}	κ_{zz}	κ_{xx}	κ_{zz}
α - Si_3N_4	68	100	224	70 ^a	105 ^b	225 ^b	-
β - Si_3N_4	73	199	237	250 ^a	170 ^b	450 ^b	69 ^c 180 ^c
γ - Si_3N_4	77	-	296	80 ^a	-	-	-

^a Ref. 19, Slack model.

^b Ref. 12, molecular dynamics (Green-Kubo).

^c Ref. 13, single crystalline grains of poly-crystals.

The directional averages $\sum_i \kappa_{ii}/3$ are 79, 115, and 77 $\text{Wm}^{-1}\text{K}^{-1}$ for the α , β , and γ phases, respectively. The value of the γ phase is similar to that of the α phase, in spite of comparatively large difference among the bulk moduli (B) that are also shown in Table II.

Table II also lists the previously reported experimental¹³ and theoretical¹² thermal conductivities for the references. Previously Morelli *et al.*¹⁹ employed the Slack model to estimate the lattice thermal conductivities of the three phases. They are shown as κ in Table II. For the β phase, our κ agrees better with the experimental, than that of the molecular dynamics¹² does. Also, our directional average $\sum_i \kappa_{ii}/3$ is much closer to the experimental average, than the κ of the Slack model.

Fig. 2 shows the theoretical κ of the α and β phases as a function of T , together with the reference experimental data^{5,11}. The thermal conductivities for a series of temperatures were only reported on the polycrystalline bulk samples and measured by the laser flash method. These thermal conductivities (denoted as $\kappa_{\text{polycrystal}}$) cannot be directly compared with the calculated intrinsic κ because they largely depended on the microstructure of the samples: They were deviated from the simple directional averages of the intrinsic κ_{ii} , depending on the shapes of the crystal grains. We treated this effect by using a parameter $0 \leq w \leq 1$ and fitting the quantities of $w\kappa_{xx} + (1-w)\kappa_{zz}$ to the experimental $\kappa_{\text{polycrystal}}$ by the least squares method. We consider these as theoretical $\kappa_{\text{polycrystal}}$.

In Fig. 2, the κ_{ii} calculated without $\tau_{\lambda, \text{bs}}$ are nearly proportional to T^{-1} because n_λ in Eq. (1) can be reduced to $\exp(-\hbar\omega_\lambda/k_B T)$. In Fig. 2-a, the experimental $\kappa_{\text{polycrystal}}$ of a chemically vapor-deposited α - Si_3N_4 sample¹¹ is not proportional to T^{-1} and intersects the theoretical κ_{ii} . Thus no value of w adjusts the theoretical conductivities to the experimental data. The full solution of LBTE would negligibly cure the disagreement. Including the simple phonon lifetime of boundary scattering, $\tau_{\lambda, \text{bs}} = L/|\mathbf{v}_\lambda|$, into the total phonon lifetime according to Matthiessen's rule, could not explain the discrepancy as well. A L value of 0.6 μm , which was much smaller than the experimental grain size¹¹ of 10 μm , decreased

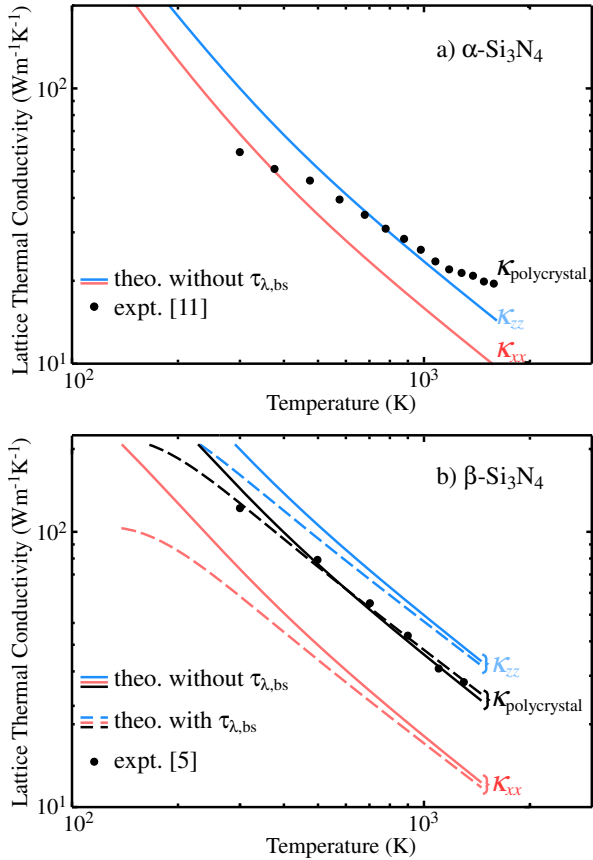


FIG. 2. (color online) Temperature dependence of thermal conductivities for α - and β - Si_3N_4 . For β - Si_3N_4 , theoretical results with the boundary scattering effect are shown by broken lines. Theoretical $\kappa_{\text{polycrystal}}$ (see in text) for the β - Si_3N_4 sample are also shown to be compared with the experimental conductivities.

the theoretical κ_{ii} in the low temperature side toward the experimental values, but severely underestimated in the high temperature side. At present, the reason for the discrepancy between the theoretical and experimental behaviors is unclear. Although the crystal structure of the experimental sample was characterized as α - Si_3N_4 , significant lattice defects existed in the as-deposited sample as pointed out by Hirosaki *et al.*¹² and the simple phonon boundary scattering model may fail to describe their effects on the $\kappa_{\text{polycrystal}}$.

The experimental $\kappa_{\text{polycrystal}}$ of the β phase are located in-between the theoretical κ_{xx} and κ_{zz} , being nearly proportional to T^{-1} . Simple directional averages of the theoretical κ_{ii} slightly underestimate these experimental values. This is understood from the fact that the microstructure was controlled to increase the $\kappa_{\text{polycrystal}}$, and the crystalline grains were selectively grown along the c axis of the most conductive direction.⁵ The theoretical $\kappa_{\text{polycrystal}}$ were fit well with $w = 0.44$ to the experimental. For the effects of lattice defects most of which were grain boundaries, we included $\tau_{\lambda,\text{bs}}$ with $L = 0.6$

μm to further fit the theoretical curve ($w = 0.33$) to the experimental data. The L value is slightly smaller than the average grain size⁵ of $2 \mu\text{m}$ in the experiment.

B. Dispersion curves

Figure 3 shows the phonon band diagrams of the three Si_3N_4 phases. The entire band diagrams are almost identical to those reported earlier^{18,41}. However, here we investigate the gradients of the band dispersions, that is, the group velocities projected on the high-symmetry paths. We especially focus on their anisotropy in the α and β phases. This was not investigated by the previous works.

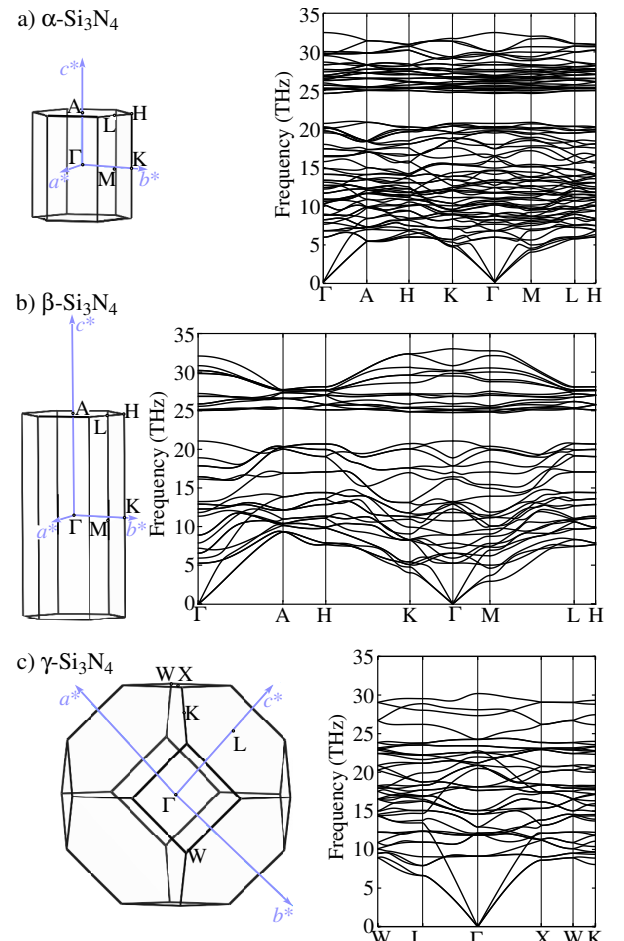


FIG. 3. (color online) Brillouin-zones (left) and calculated phonon band diagrams (right) for three Si_3N_4 phases.

In Fig.3-b, the acoustic branches in the β phase increase ω_λ much more from Γ to A than from Γ to K or M . In Fig.3-a of the α phase, ω_λ increase similarly among the paths. This is due to the different Γ - A path lengths. The β phase has an approximately twice longer path than the α phase; the lattice constant c of the β phase is nearly half that of the α phase, owing to the difference

in the stacking manner of the basal layer structures. The anisotropic dispersions indicate large anisotropy in the \mathbf{v}_λ . This will be investigated further in the following sections. Normally, optical branches are flat; however, the β phase shows significantly large gradients of the band dispersions of the low frequency optical phonon branches. This indicates that the phonon modes on these branches have large \mathbf{v}_λ as well.

In the γ phase, the acoustic phonon branches show significant linear dispersions on the Γ -L and Γ -X paths. Their roughly constant gradients are large, reflecting the large bulk modulus of the γ phase as shown in Table II.

C. ω_λ counter map on reciprocal plane

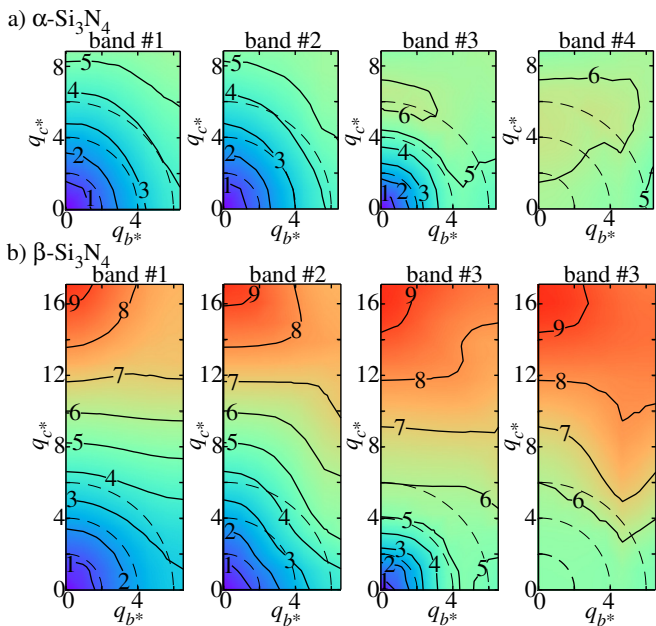


FIG. 4. (color online) Contour maps of phonon frequency (THz) on the b^*c^* planes of Brillouin-zones. The coordination in the reciprocal plane are in units of 10^{-2} \AA^{-1} . The maps for the four lowest-frequency phonon states are shown. The frequency landscapes are formed by simply connecting the frequencies of the same band indices, assigned by ascending order of frequency at the respective \mathbf{q} points.

We investigate the anisotropy in \mathbf{v}_λ by using another geometry, that is, a cross-section of the Brillouin-zone. Fig. 4 shows counter maps of ω_λ on the b^*c^* plane. We show the counter maps for the four lowest-frequency bands, because they contribute significantly to the κ . There were negligible differences between the distributions on the b^*c^* plane and the other planes containing the c^* axis. Thus we select the b^*c^* plane as a representative. In the α phase, the distributions are nearly isotropic. The group velocities are thus nearly isotropic. In the β phase, the iso-frequency lines in $0.06 \leq q_{c^*} \leq 0.12 \text{ \AA}^{-1}$ are rather parallel to the q_b^*

axis. The \mathbf{v}_λ orient closely to the c^* axis direction. This confirms the large anisotropy in \mathbf{v}_λ of the acoustic and low-frequency optical branches in the β phase.

D. Frequency-dependences of κ^c , \mathbf{v}_λ and Γ_λ

We have investigated in the previous two sections the anisotropy in \mathbf{v}_λ , which can explain the anisotropy in the κ . Here we completely investigate the characteristic points in the κ by using the phonon properties existing in the closed form of RTA in Eq. (2). These properties are taken over the Brillouin zone, similar to κ . In order to investigate these properties with respect to the phonon modes, we show in Fig. 5 frequency distributions of these properties: Phonon densities of states (DOS) in Fig. 5-a are viewed as frequency distributions of heat carriers. In Fig. 5-a peaks at the lowest frequency within the DOS are denoted by arrows. Considering the band diagrams, these peaks are approximately associated with flattening of acoustic branches near Brillouin zone boundaries. In Fig. 5-c, κ^c and their first derivatives are shown in order to find the phonon mode contribution to the κ clearly. In Fig. 5-c, we weighted the DOS with $v_{\lambda,i}^2$. They show both of the impacts of $v_{\lambda,i}$ and number of heat carriers. We abbreviate these weighted DOS as WDOS. Phonon linewidths are a remaining important property. They are shown as scatter plots ($\Gamma_\lambda, \omega_\lambda$) in Fig. 5-d.

Among the panels in Fig. 5, the γ phase has its DOS, WDOS, and Γ_λ distribution much different from the others, consistently with the large differences in the crystal structure. Some of the remarkable differences may be explained by its characteristic chemical bonding: (1) The DOS peak is located at the highest frequency among the three phases. This is consistent with the band diagram showing the linear dispersions of the acoustic phonon branches with the large gradients. This is related to the strong chemical bonding by the large bulk modulus. Reflecting this feature, in the lower frequency side of the peak, the DOS has the lowest intensities among the three phases. This means the smallest distribution of heat carriers. (2) At most of the frequencies with phonon modes largely contributing to κ , the WDOS is the next largest to the one for $v_{\lambda,z}$ of the β phase. This is also explained by the large gradients in the acoustic phonon branches. (3) At these frequencies, the linewidths are the largest among the three phases. For this point, we investigate the three-phonon-scattering strength $\Phi_{\lambda\lambda'\lambda''}$. In Table. III, the magnitudes of $\Phi_{\lambda\lambda'\lambda''}$ are compared as their averages over two kinds of frequency ranges for ω_λ and all indices in λ' and λ'' . Its average over ω_λ in 0–15 THz is much larger than that of the other phases. This explains the largest linewidths. Owing to these linewidths and DOS, the κ_{xx}^c is not so large and resembles the κ_{xx}^c of the β phase.

We hereafter compare the properties between the α and β phases. It is interesting that κ^c in the β phase still increase significantly in the higher frequency side of

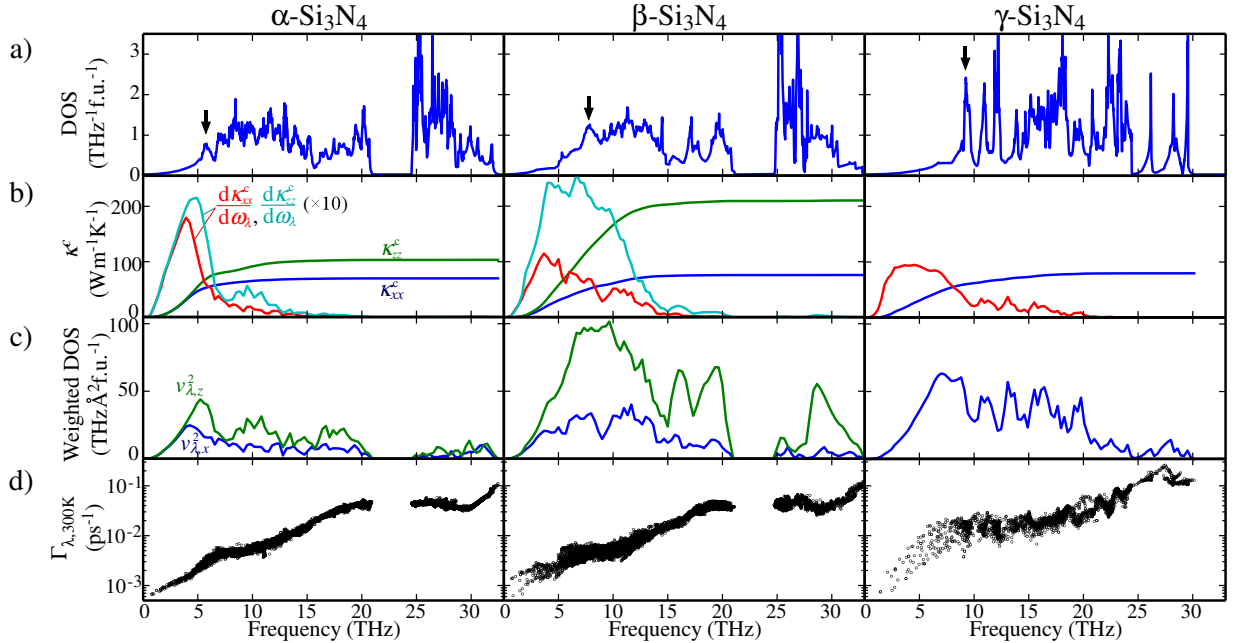


FIG. 5. (color online) Microscopic phonon properties of three Si_3N_4 phases. Cumulative thermal conductivity κ^c and its derivative (a), DOS (b), weighted DOS with $v_{\lambda,i}^2$ (c) and linewidth Γ_λ (d).

TABLE III. Averages of $\Phi_{-\lambda\lambda'\lambda''}$ over frequency ranges of ω_λ (0–15 and 0–35 THz) and all (λ', λ') . The values are in units of $10^{-10} \text{ eV}^2 \text{f.u.}^{-1}$.

Frequency Range (THz)	Phase		
	α	β	γ
0–15	2.66	2.63	5.76
0–30	13.1	13.0	11.4

the DOS peak. In this frequency range, WDOS of the β phase show still large intensities. The linewidths as well as DOS are not differently distributed between the two phases. The DOS are the case as well. Thus the significant increase in κ^c in the higher frequency side of the DOS peak is ascribed only to the large v_λ . The large v_λ in this frequency range are consistent with the band diagram we have investigated. In Figs. 5-b and c, the profiles of $\frac{d\kappa_{ii}^c}{d\omega_\lambda}$ are qualitatively explained by the WDOS with $v_{\lambda,i}^2$, with the same directional indicies. Because DOS and Γ_λ are similar between the phases, the v_λ simply account for the different anisotropy in κ .

It is still curious that Γ_λ are similar between these phases although v_λ have marked differences. We investigate this further. As for not Γ_λ but a lattice thermal conductivity, Lindsay *et al.*⁴² found its significant positive correlation with the number of configurations for the three phonons, $\{\lambda, \lambda', \lambda''\}$ (the phase space available for the three-phonon scattering), among many crystals of the zincblende structure. Closely related to this, as for Γ_λ , Γ_λ directly depends on the number of configurations

for the available two phonons, $\{\lambda', \lambda''\}$, through the formula of Γ_λ which contains delta functions corresponding to the selection rule of the three-phonon scattering¹⁵. A distribution of the configurations is represented as a joint density of states (JDOS), $D_2(\mathbf{q}, \omega)$,

$$D_2(\mathbf{q}, \omega) = D_2^{(1)}(\mathbf{q}, \omega) + D_2^{(2)}(\mathbf{q}, \omega) \quad (4)$$

where

$$\begin{aligned} D_2^{(1)} &= \frac{1}{N} \sum_{\lambda' \lambda''} \Delta(-\mathbf{q} + \mathbf{q}' + \mathbf{q}'') \\ &\times [\delta(\omega + \omega_{\lambda'} - \omega_{\lambda''}) + \delta(\omega - \omega_{\lambda'} + \omega_{\lambda''})], \\ D_2^{(2)} &= \frac{1}{N} \sum_{\lambda' \lambda''} \Delta(-\mathbf{q} + \mathbf{q}' + \mathbf{q}'') \\ &\times \delta(\omega - \omega_{\lambda'} - \omega_{\lambda''}), \end{aligned}$$

with $\Delta(\mathbf{x})$ giving 1 if \mathbf{x} is a reciprocal lattice vector and otherwise zero. JDOS were employed to analyze the linewidths of $\text{Ge}_2\text{Sb}_2\text{Te}_5$ ⁴⁰ and the imaginary parts of the self energy of many zincblende and wurtzite polymorphs¹⁵. Following to these studies, we employ the JDOS to examine the similarity between the Γ_λ of the α and β phases.

Fig. 6 shows frequency-functions of JDOS at different \mathbf{q} -points on the Γ -A and Γ -K paths. They have very weak \mathbf{q} -point dependences. At the low frequency region with phonon modes largely contributing to the κ , among the two terms of $D_2^{(1)}$ and $D_2^{(2)}$ in Eq. (4), dominant is $D_2^{(2)}$. The $D_2^{(2)}$ basically corresponds to the half part ($\omega \geq 0$) of the auto-correlation function of the DOS.

The DOS for both of the α and β phases in Fig. 5-a have a frequency gap. The $D_2^{(2)}$ reflect this DOS feature, dropping suddenly around 0 THz and showing a small shoulder around 5 THz, which corresponds to the width of the gap. Moreover the $D_2^{(2)}$ shows a broad peak around 18 THz, which corresponds to the frequency shift to make the largest correlation between the DOS in the higher and lower frequency portions of the gap. Because the gap is originated from the differences in the vibrations of the planer NSi₃ contained in both of the α and β crystal structures,⁴¹ the major shapes of the $D_2^{(2)}$, reflecting this gap feature, are similar in these phases. In summary, the fraction of the acoustic and low frequency optical phonon modes is not large. Therefore JDOS at their frequencies are mainly determined by the other many phonon modes. Table. III indicates that the $\Phi_{\lambda\lambda'\lambda''}$ are similar between the two phases. With these similar impacts of the JDOS and $\Phi_{\lambda\lambda'\lambda''}$, Γ_λ in Fig. 5-d are similar.

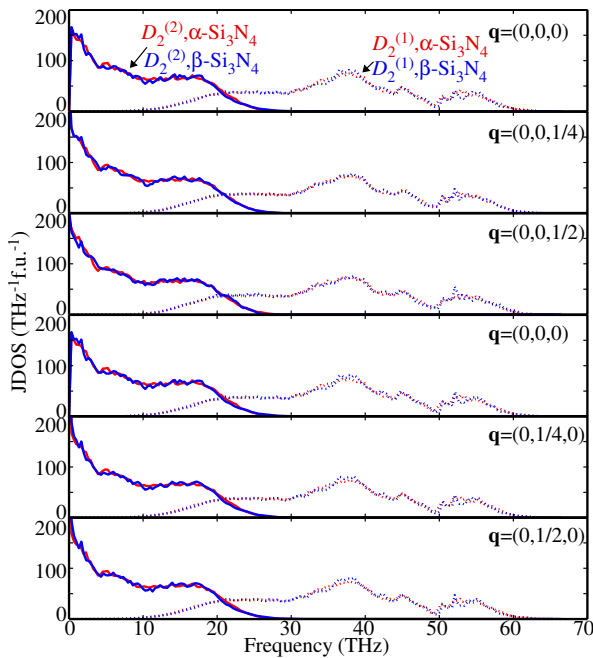


FIG. 6. (color online) JDOS of α - and γ -Si₃N₄ at different \mathbf{q} points. The first and forth rows are JDOS at the same Γ -point but calculated with the polarization for non-analytic term correction set along c^* and b^* , respectively.

In Fig. 5-d, as a small but interesting difference in linewidths distributions, Γ_λ below 5 THz are aligned on a single smooth line in the α phase, while those in the β phase are scattered roughly on two lines. This difference is investigated with directions of the atomic vibrations of the phonon modes. Fig. 7 enlarges the $(\Gamma_\lambda, \omega_\lambda)$ in this frequency range. In Fig. 7-a, the Γ_λ are classified using colors according to the sums of the squares of the eigenvector components along the \mathbf{q} ; the sum is 1 for a perfectly longitudinal wave. However, these sums have no clear color-contrast to distinguish the two branches in the β phase. Fig. 7-b shows the same plot as Fig. 7-a, but

with colors according to the sums of the squares of the eigenvector components along the ab plane, which has 1 when the eigenvectors lie on the ab plane. There is a tendency in the β phase that Γ_λ are large for vibrations along the ab plane. Therefore, within the single-mode RTA, for the phonon modes below 5 THz, all of which belong to the acoustic phonon branches, vibration modes along the ab plane are more easily scattered in the β phase, no matter whether they are longitudinal or transverse. For the panel of β -Si₃N₄ in Fig. 7-b, a straight line can divide the phonon modes into the two groups. The numbers of the phonon modes in the upper and lower parts are 157 and 58, whose ratio is consistent to the population ratio of the vibration modes along and out of the ab plane.

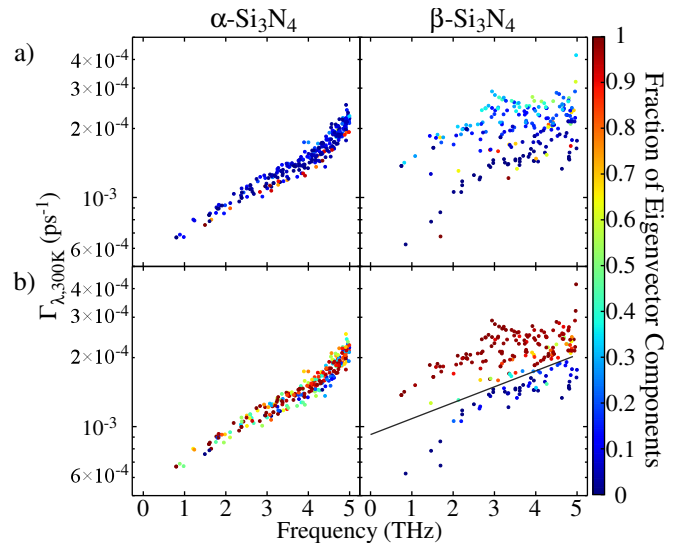


FIG. 7. (color online) Distribution of linewidths $\omega_\lambda \leq 5$ THz with colormaps with respect to strengths of eigenvector components along \mathbf{q} (a) and on a - b plane (b).

IV. SUMMARY

In the present study, we investigate the lattice thermal conductivities of the three Si₃N₄ phases, by using the lattice dynamics based on the *ab-initio* interatomic force constants. The main remarks are as follows:

1) In the α - and β -Si₃N₄, whose crystal structures are characterized by the stacking manners of the basal layer structures, which largely alter κ . In α -Si₃N₄, the κ are rather isotropic, while the κ_{zz} in the β phase is twice or more larger than the other κ_{ii} in the three phases.

2) In the α phase, the acoustic mode phonons below 6 THz are the main heat carriers, while in the β phase, the phonons below 12 THz contribute to the κ . The group velocities alone qualitatively explain this and the different behaviours in κ between these phases. This is partly because JDOS is insensitive to the group velocities of a small fraction of phonon modes.

3) In the γ phase, the κ_{xx} is relatively small. The κ_{xx}^c is similar to that of $\beta\text{-Si}_3\text{N}_4$. Its large linewidths and small number of heat carriers explain this.

ACKNOWLEDGMENTS

The present work was partly supported by Grants-in-Aid for Scientific Research of MEXT, Japan (Grant No. 15K14108 and ESISM (Elements Strategy Initiative for Structural Materials) of Kyoto University).

Appendix A: Pressure dependence of LTC of γ -phase

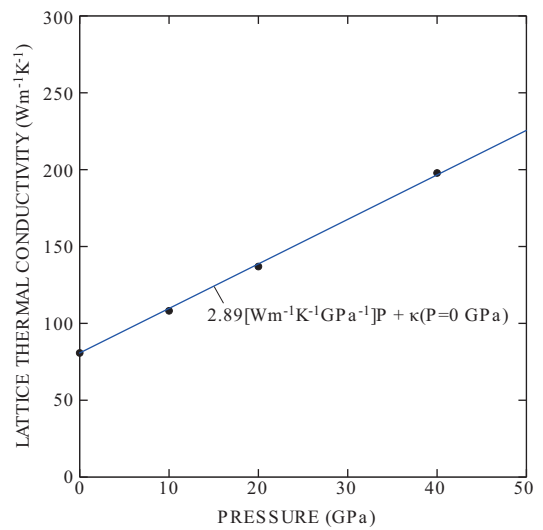


FIG. 8. (color online) Pressure dependence of LTC of $\gamma\text{-Si}_3\text{N}_4$.

- * k-tatsumi@imass.nagoya-u.ac.jp
- ¹ G. Slack, Journal of Physics and Chemistry of Solids **34**, 321 (1973).
- ² Y. Zhou, H. Hyuga, D. Kusano, Y.-i. Yoshizawa, and K. Hirao, Advanced Materials **23**, 4563 (2011).
- ³ K. Hirao, K. Watari, H. Hayashi, and M. Kitayama, MRS Bulletin **26**, 451 (2001).
- ⁴ K. Watari, Journal of the Ceramic Society of Japan **109**, S7 (2001).
- ⁵ N. Hirosaki, Y. Okamoto, M. Ando, F. Munakata, and Y. Akimune, Journal of the Ceramic Society of Japan **104**, 49 (1996).
- ⁶ F. L. Riley, Journal of the American Ceramic Society **83**, 245 (2000).
- ⁷ M. Yashima, Y. Ando, and Y. Tabira, The Journal of Physical Chemistry B **111**, 3609 (2007).
- ⁸ D. Du Boulay, N. Ishizawa, T. Atake, V. Streltsov, K. Furuya, and F. Munakata, Acta Crystallographica Section B: Structural Science **60**, 388 (2004).
- ⁹ S. Hampshire, H. Park, D. Thompson, and K. Jack, Nature **274**, 880 (1978).
- ¹⁰ T. Hahn, ed., International tables for crystallography, Vol. A (John Wiley & Sons, Inc., 2011).
- ¹¹ T. Hirai, S. Hayashi, and K. Niihara, AM. CERAM. SOC. BULL. Am. Ceram. Soc. Bull. **57**, 1126 (1978).
- ¹² N. Hirosaki, S. Ogata, C. Kocer, H. Kitagawa, and Y. Nakamura, Physical Review B **65**, 134110 (2002).
- ¹³ B. Li, L. Pottier, J. Roger, D. Fournier, K. Watari, and K. Hirao, Journal of the European Ceramic Society **19**, 1631 (1999).
- ¹⁴ R. Vashishta, R. K. Kalia, A. Nakano, and I. Ebbssö, Amorphous Insulators and Semiconductor, edited by M. F. Thorpe and M. I. Mitkova (Kluwer, 1996).
- ¹⁵ A. Togo, L. Chaput, and I. Tanaka, Physical Review B **91**, 094306 (2015).
- ¹⁶ A. Zerr, G. Miehe, G. Sergheiou, M. Schwarz, E. Kroke, R. Riedel, H. Fueß, P. Kroll, and R. Boehler, Nature **400**, 340 (1999).
- ¹⁷ Y. Zhang, A. Navrotsky, and T. Sekine, Journal of materials research **21**, 41 (2006).
- ¹⁸ B. Xu, J. Dong, P. F. McMillan, O. Shebanova, and A. Salamat, Physical Review B **84**, 014113 (2011).
- ¹⁹ D. Morelli and J. Heremans, Applied Physics Letters **81**, 5126 (2002).
- ²⁰ L. Chaput, Physical review letters **110**, 265506 (2013).
- ²¹ S.-i. Tamura, Physical Review B **27**, 858 (1983).
- ²² A. Togo and I. Tanaka, Scripta Materialia **108**, 1 (2015).
- ²³ P. E. Blöchl, Phys. Rev. B **50**, 17953 (1994).
- ²⁴ G. Kresse and J. Furthmüller, Physical review B **54**, 11169 (1996).
- ²⁵ G. Kresse, J. Non-Cryst. Solids **193**, 222 (1995).
- ²⁶ D. J. Kresse, Georg, Phys. Rev. B **59**, 1758 (1999).
- ²⁷ J. P. Perdew, K. Burke, and M. Ernzerhof, Phys. Rev. Lett. **77**, 3865 (1996).
- ²⁸ W. Paszkowicz, R. Minikayev, P. Piszora, M. Knapp, C. Bähitz, J. Recio, M. Marques, P. Mori-Sánchez, L. Gerward, and J. Jiang, Phys. Rev. B **69**, 052103 (2004).
- ²⁹ D. M. Ceperley and B. Alder, Physical Review Letters **45**, 566 (1980).
- ³⁰ S. Wei and M. Chou, Physical review letters **69**, 2799 (1992).
- ³¹ Y. Wang, J. Wang, W. Wang, Z. Mei, S. Shang, L. Chen, and Z. Liu, J. Phys.: Condens. Matter **22**, 202201 (2010).

- ³² M. Gajdoš, G. Hummer, G. Kresse, J. Furthmüller, and B. F, Phys. Rev. B **73**, 045112 (2006).
- ³³ X. Wu, D. Vanderbilt, and D. R. Hamann, Phys. Rev. B **72**, 035105 (2005).
- ³⁴ M. T. Dove, *Introduction to lattice dynamics*, Vol. 4 (Cambridge university press, 1993) pp. 76–77.
- ³⁵ A. Ward and D. Broido, Physical Review B **81**, 085205 (2010).
- ³⁶ R. Minikayev, W. Paszkowicz, P. Piszora, M. Knapp, and C. Bähtz, “Thermal expansion of and silicon nitride,” (2007).
- ³⁷ P. Andersson, Journal of Physics C: Solid State Physics **18**, 3943 (1985).
- ³⁸ A. Cepellotti and N. Marzari, Physical Review X **6**, 041013 (2016).
- ³⁹ R. J. Hardy, Physical Review B **2**, 1193 (1970).
- ⁴⁰ S. Mukhopadhyay, L. Lindsay, and D. J. Singh, Scientific reports **6** (2016).
- ⁴¹ A. Kuwabara, K. Matsunaga, and I. Tanaka, Physical Review B **78**, 064104 (2008).
- ⁴² L. Lindsay and D. A. Broido, J. Phys.: Condens. Matter **20**, 165209 (2008).